Hybrid simulation of foreshock waves and ion spectra and their linkage to cusp energetic ions

X. Y. Wang,[1] Y. Lin,[1] and S.-W. Chang[2,3]

Received 10 September 2008; revised 13 March 2009; accepted 19 March 2009; published 3 June 2009.

[1] A three-dimensional global hybrid simulation is carried out to investigate energetic ions and electromagnetic waves in the quasi-parallel (Q-||) bow shock and cusp for a typical interplanetary magnetic field configuration during the cusp energetic particle events. The bow shock, magnetosheath, and dayside magnetosphere form by interaction between the solar wind and geomagnetic dipole field. Ions of solar wind characteristics injected into the system evolve along with electromagnetic waves in a self-consistent manner. Several important features are yielded from the simulation. Solar wind ions are accelerated by the waves and turbulence at the bow shock and foreshock as indicated by the ion distribution. The shock-accelerated ions possess an exponential energy spectrum with their differential flux scaled by the field-aligned distance to the bow shock, consistent with satellite observations. Second, the compressive and transversal waves in the foreshock are strongly correlated with the diffuse ion dynamics. Third, energetic ions in the magnetosheath and cusp downstream from the Q-|| shock also exhibit a spectrum similar to those at the shock. By tracing trajectories of cusp energetic ions in the simulation, the origin of these ions is revealed. Their source is predominantly associated with the Fermi acceleration at the Q-|| shock and foreshock. Waves in the magnetosheath and cusp, as well as magnetic reconnection at the high-latitude magnetopause, are relatively insignificant in accelerating cusp energetic particles.

Citation: Wang, X. Y., Y. Lin, and S.-W. Chang (2009), Hybrid simulation of foreshock waves and ion spectra and their linkage to cusp energetic ions, *J. Geophys. Res.*, *114*, A06203, doi:10.1029/2008JA013745.

1. Introduction

[2] The magnetic cusp is generally regarded as a funnel shape region in the high-latitude dayside magnetosphere. In this region, magnetic field lines are usually open, allowing direct entry of the magnetosheath particles into the magnetosphere [*Heikkila and Winningham*, 1971; *Smith and Lockwood*, 1996]. The geometry and temporal structure of the cusp have been extensively studied using quantitative modeling [*Tsyganenko and Russell*, 1999], empirical modeling [*Fenrich et al.*, 2001], MHD simulations [*Siscoe et al.*, 2005, 2007], and satellite observations [e.g., *Zong et al.*, 2005; *Cargill et al.*, 2005]. Structure of magnetic field and plasma characteristics are often utilized to identify the cusp in satellite observations. In addition, particle distributions and energy spectra also provide important information on the dynamics of the cusp.

[3] Besides the shocked solar wind ions, energetic ions with energies from 10 keV up to 1 MeV have been reported in the cusp [e.g., *Chen et al.*, 1997]. These energetic particles could play an important role in the geospace environment that they may bounce and/or transport away from the cusp entering other regions in the magnetosphere. The quest to understand the origin of the cusp energetic particles (CEPs) has generated a series of debates [e.g., *Fritz and Chen*, 1999; *Trattner et al.*, 1999, 2003; *Chen et al.*, 2003; *Chang et al.*, 2003; *Sheldon et al.*, 2003]. It has been argued that CEPs are accelerated locally by ULF waves [*Chen et al.*, 1998]. On the other hand, it has been suggested that cusp energetic ions are originated from leakage of magnetospheric energetic ions [*Blake*, 1999]. Nevertheless, the presence of energetic O^+ in the cusp could imply either one of the above sources or both [*Lavraud et al.*, 2005; *Vogiatzis et al.*, 2008]. In addition, a bow shock source has been proposed that the bulk of CEPs are originated in the solar wind and accelerated upstream by the quasi-parallel (Q-||) bow shock [*Chang et al.*, 1998]. Energy spectrum of CEPs agrees well with those of the typical bow shock diffuse ions. Moreover, CEPs have density and temperature distributions similar to the upstream values [*Trattner et al.*, 2001].

[4] It is well know that energetic ions are ubiquitous upstream and downstream from the Q-|| bow shock. Observations show that ions at the Q-|| shock contain a Maxwellian core distribution and a "diffusive" tail distribution with energies up to hundreds of keVs [e.g., *Ipavich et al.*, 1981; *Möbius et al.*, 1987; *Gosling et al.*, 1989; *Ellison et al.*, 1990; *Fuselier et al.*, 1995; *Cao et al.*, 2009]. A theoretical model has been used to derive the relation between the upstream

[1]Physics Department, Auburn University, Auburn, Alabama, USA.
[2]Center for Space Plasma and Aeronomic Research, University of Alabama in Huntsville, Huntsville, Alabama, USA.
[3]National Space Science and Technology Center, Huntsville, Alabama, USA.

0148-0227/09/2008JA013745

hydromagnetic waves and "diffuse" ions [*Lee*, 1982]. This result is verified by a statistical study of AMPTE/IRM data [*Trattner et al.*, 1994]. One-dimensional hybrid simulations have also been used to elucidate the origin of diffuse ions [e.g., *Scholer and Terasawa*, 1990; *Trattner and Scholer*, 1994]. Recently, bow shock waves and associated ion dynamics have been investigated using two-dimensional [*Blanco-Cano et al.*, 2006] and three-dimensional (3-D) [*Lin and Wang*, 2005] global hybrid simulations. In these simulations, electromagnetic waves and diamagnetic cavities are generated in the foreshock region by interaction between the reflected, back-streaming ion beams and incoming solar wind. A hot, partially diffused ion distribution appears in the foreshock cavities.

[5] To investigate contribution from bow shock diffuse ions to CEPs, it requires a direct link between the particle dynamics in the bow shock and cusp. This presents a challenge to observation and data analysis. Hybrid simulation in a 3-D global scale is an ideal tool for this investigation. Recently, it has been shown for the first time using a 3-D global hybrid simulation to establish the linkage between the bow shock and CEPs [*Lin et al.*, 2007]. In their study, CEPs were mapped to the Q-|| shock, but their relation to the foreshock and cusp waves was not investigated.

[6] In this paper, we continue our previous study and investigate the role of bow shock in the production of CEPs using 3-D global hybrid simulations. Since waves in the Q-|| shock are vital in the generation of foreshock energetic ions, properties of waves and turbulence in the foreshock are analyzed. The relationship between the wave energy density and diffuse ion energy density is also studied. This comprehensive study further establishes the linkage between the bow shock diffuse ions and CEPs and advances our understanding of the contribution of cusp waves to CEP energy. The rest of the paper is as follows. Details of our 3-D simulation model are described in section 2. Simulation results are presented in section 3. In section 4, simulation results are compared with observations and the origin of CEPs is discussed. A summary is given in section 5.

2. Simulation Model

[7] It has been demonstrated that hybrid simulation is a powerful tool to solve physical problems in a system dominated by ion dynamics at a timescale $\omega \sim \Omega_i$ and spatial scale $k\rho_i \sim 1$, where ω is the wave frequency, k is the wave number, and Ω_i and ρ_i are the ion gyrofrequency and Larmor radius, respectively. Our 3-D global-scale hybrid code [*Lin and Wang*, 2005, 2006] has been developed following the hybrid scheme of *Swift* [1996], and has been used to investigate ion dynamics and electromagnetic waves excited at the bow shock and cusp self-consistently. In our model, protons are treated as fully kinetic particles and electrons are treated as a massless fluid, assuming quasi-charge neutrality. The simulation domain contains a hemispherical plasma region with $x > 0$ in the GSM coordinate system, and the geocentric distance r ranging from 4 R_E to 23 R_E. A spherical coordinate system is used in the calculation, in which the polar axis is along the GSM y axis and two columns of 20° semicones centered on the $\pm y$ axis are excluded.

[8] The upstream region at $r > 10$ R_E is filled with uniform solar wind and interplanetary magnetic field (IMF). Magnetic fields from a 3-D dipole occupy the region within $r < 10$ R_E [*Lin and Wang*, 2005]. A dipole tilt of 15° toward the $+x$ direction is implemented to maintain the northern cusp within the simulation domain. Solar wind is assumed to be uniform and isotropic, with $\beta_i = \beta_e$, where β_i and β_e are the ion and electron beta values, respectively. A fixed boundary condition with constant solar wind and IMF parameters is placed at the outer boundary at $r = 23$ R_E. Free boundary conditions are used at the backside planner boundaries at $x = 0$ and the two semiconic boundaries. A perfect conducting sphere of radius 4 R_E is imposed at the inner boundary.

[9] In the simulation, the ion velocities and positions are advanced in time under the influence of the electromagnetic field according to their equation of motion. The electric field is calculated from the electron momentum equation. The magnetic field is updated by the Faraday's law. In addition to the particle ions, a cold, incompressible ion fluid is assumed to dominate the inner magnetosphere at $r < 7$ R_E [*Swift*, 1996; *Lin and Wang*, 2005]. However, fully kinetic ions remain the dominant species in the region of interest. The electron fluid is assumed to be isothermal. Note that an adaptive time step is implemented for the simulation. For particles in the low-altitude cusp, where the magnetic field is strong, time step reduces to $1/n$ time step, with n being equal to half of the ratio of ion gyrofrequency to the solar wind gyrofrequency.

[10] A splitting particle method is adopted in the simulation to improve the counting statistics for more energetic ions [*Giacalone et al.*, 1992; *Lin et al.*, 2007]. In this method, when the particle energy reaches a certain threshold, this particle is split into two particles, each carrying half the mass and charge so that the total moments are conserved. An appropriate weight is assigned to each subparticle.

[11] In this study, the grid numbers in the spherical coordinate system are $136 \times 104 \times 130$, and a total number of $\sim 3 \times 10^8$ particles is used. The grids along the polar and azimuthal coordinate axes are uniform, while they are nonuniform in the radial direction. Around the regions of the magnetopause boundary layer, magnetosheath, and bow shock, the grid size $\Delta r \sim 0.1$ R_E, approximately equals to the solar wind ion inertial length. The solar wind number density N_0 is chosen to be $12{,}000/R_E^3$, corresponding to about 150–450 particles per cell. A massively parallel computation is performed. Note that the magnetospheric ions recycled from the nightside are not included in the present model.

[12] For the presentation below, length is expressed in R_E. Time is normalized to Ω_{i0}^{-1}, where $\Omega_{i0} = eB_0/m_i$ is the solar wind ion gyrofrequency and it is chosen to be the typical value, 1 s^{-1}. The ion velocity, density, temperature, magnetic field and electric field are normalized to solar wind Alfvén speed (V_{A0}), solar wind density (N_0), $m_i V_{A0}^2$, IMF B_0 and $V_{A0}B_0$, respectively.

3. Simulation Results

[13] The simulation has been performed for cases with various solar wind Mach number $M_A = 3$–9, and IMF cone angle = 0°, 15°, and 30°. In the following, we focus our presentation on the case with $M_A = 8$, IMF $\mathbf{B}_0 = (-0.966, 0, 0.259)$ with a 15° IMF cone angle, and the solar wind ion beta $\beta_i = 0.5$. Such an IMF geometry corresponds to a

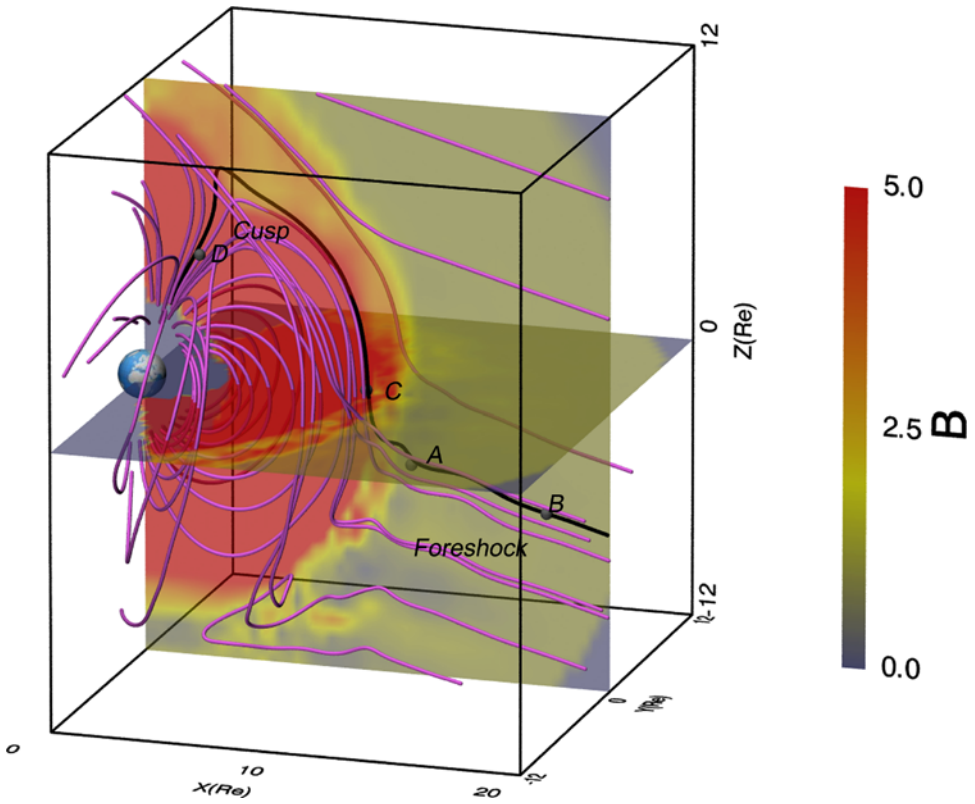

Figure 1. Magnetic field lines in 3-D perspective and magnetic field B in the noon-meridian and equatorial planes at $t = 100$. Locations A and B are in the foreshock region at colatitude $\theta = 105°$ and $r = 12$ and 18, respectively. Region C is in the magnetosheath at $r = 10$ and $\theta = 90°$. Region D is in the cusp at $r = 5.5$ and $\theta = 30°$. Regions A, B, C, and D are roughly connected by the same field line.

typical configuration during the CEP events [*Chang et al.*, 2000].

[14] The bow shock, magnetosheath, and magnetopause begin to form at time about $t = 20$ in the simulation, and they are nearly stationary at $t \geq 30$. The nose of bow shock is about $x = 12\ R_E$, and that of the magnetopause boundary is about $x = 9.6\ R_E$.

[15] Figure 1 presents several magnetic field lines in 3-D perspective and the field magnitude in the noon-meridian and equatorial planes at $t = 100$. From the field line geometry, it is clear that the southern hemisphere position of the bow shock within $-12 \leq z \leq 0$ is near parallel or Q-$\|$. Intense fluctuations in magnetic field appear in the foreshock region. Slightly weaker waves also exist in the cusp. The cusp field lines form a 3-D funnel-shape volume, which is filled with dense magnetosheath particles. As shown by the 3-D field lines in Figure 1, the northern cusp and the Q-$\|$ bow shock are connected by **B** field lines through high-latitude reconnection tailward of the cusp (see, e.g., the black field line in Figure 1). Ions originated from the solar wind can travel along these field lines, pass through the magnetosheath and then directly enter the cusp. Our study focuses on particle and wave properties in several regions. They are presented below in the order from upstream to downstream.

3.1. Ion Signatures at the Q-$\|$ Shock

[16] Ion distributions at two locations in the Q-$\|$ shock and foreshock as labeled by A and B in Figure 1 are present in Figure 2 (left and middle). These two points are selected within the same magnetic flux tube for analysis. Characteristics in ion distribution can be deduced from these two scatterplots, one in $v_{\|} - v_{\perp 1}$ plane and the other in $v_{\perp 2} - v_{\perp 1}$ plane, where $\mathbf{v}_{\|}$ is along **B**, $\mathbf{v}_{\perp 1}$ is parallel to $\mathbf{B} \times \mathbf{e}_y$, and $\mathbf{v}_{\perp 2}$ is perpendicular to the above two directions, ie. $\mathbf{v}_{\|} \times \mathbf{v}_{\perp 1}$. Figure 2 (right) shows the ion energy spectra, ion differential number flux I_p versus ion energy E_p, where $I_p = Ef$, and f is the ion distribution function.

[17] Three distinct populations appear in region A at the Q-$\|$ shock, as shown in Figure 2 (top). They are the incident solar wind ions flowing earthward, with $V_{p\|} \simeq 7.72$, reflected gyrating ions characterized by a beam-like distribution with a sunward flow, and more energetic and gyrotropic ions (diffuse ions). The first two ion populations form a thermal distribution and the last one constitutes the energetic tail as illustrated in the ion energy spectrum in Figure 2. The energetic component is well fitted by an exponential function with an *e*-folding energy ~90.

[18] Father away from the Q-$\|$ shock, ion distribution at point B in the upstream region differs from the one at point A. Instead of three populations at A, there are only two at B, namely the solar wind ions and the diffuse ions as shown in Figure 2 (bottom). The coherent, gyrating ions reflected at the shock gradually disappear or evolve into the diffuse ions as they travel upstream. While the energetic ions at point A have a partial gyrotropic distribution, those at B are nearly completely gyrotropic. Moreover, similar to the bow shock ion energy spectrum at point A, the foreshock ion spectrum at point B consists of the thermal component and the

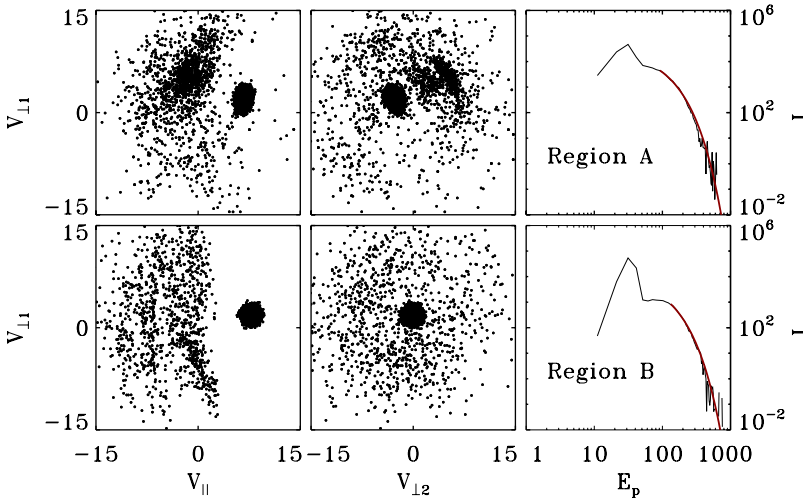

Figure 2. Scatterplots of ion velocity distributions in the (left) $v_{\parallel} - v_{\perp 1}$ and (middle) $v_{\perp 2} - v_{\perp 1}$ planes and (right) ion energy spectra in regions (top) A and (bottom) B in the foreshock. The red curve indicates the exponential fits for the energetic ion spectra.

energetic tail. The latter, with energy extending to $20E_{sw}$, where $E_{sw} = 32$ is the solar wind proton energy, is also well described by an exponential function with an *e*-folding energy of 99.

[19] By comparing two energy spectra in Figure 2, one can immediately tell that energetic ion flux reduces at different rate for a different energy as ions move further upstream. Along the magnetic flux tube connecting A and B, energetic ion flux is scaled by an exponential function with an *e*-folding distance that is energy-dependent. Figure 3 presents this *e*-folding distance s_0 at various ion energy E_p. It increases with ion energy more rapidly until ion energy is greater than 120.

3.2. Waves in the Q-‖ Shock

[20] In the simulations, there are two types of electromagnetic waves upstream from the Q-‖ shock, the transversal Alfvénic and the whistler types [*Lin and Wang*, 2005]. Similar to those shown in a previous study [see *Lin and Wang*, 2005, Figure 4], fluctuations in B are well correlated with those in the flow velocity in both y and z components. These waves propagate mainly along the magnetic field, with wave number $k \simeq 1-2$ and a sunward velocity $V_s \sim 3$ in the solar wind frame, but are carried earthward by the solar wind at a speed of 5. Furthermore, wave amplitude decreases farther away from the shock. The maximum amplitude $|\delta B| \sim 1$ is near the shock front. These upstream waves are generated by the nonlinear interaction of back-streaming ions (beam-like) with the solar wind [*Lin and Wang*, 2005] via the so-called beam-plasma interaction process [*Wang and Lin*, 2003], while compressive waves near the shock are generated by gyrating ion beams [*Blanco-Cano et al.*, 2006].

[21] Figure 4 shows wave power (W) in B_y (transversal waves) and total B (compressive waves) for a range of wave frequency (ω) and upstream distance (s). The wave power, calculated by applying a fast Fourier transformation to the magnetic field data obtained within $t = 50-100$, generally decreases with s. The transversal wave is right-hand polarized, with maximum power at $\omega \simeq 0.5$. Additional but much weaker peaks appear near the shock front, at $\omega \simeq 0.125$ and 1. The compressive wave, however, shows two dominant frequencies at $\omega \simeq 0.25$ and 0.75. In the region of $s = 2-5$, this wave component also exhibits a significant strength at $\omega = 0.125$, 0.5, and 1.

[22] Wave energy densities for both the transversal and compressive waves, acquired by integrating wave power $W(\omega, s)$ over ω, decrease with s. The power density of the transversal wave is nearly 5 times the compressive wave power. The energy density of transversal component decreases nearly exponentially with s, with an *e*-folding distance of 3. The energy density of the compressive wave is enhanced significantly near shock front in region $s = 0.5-2$.

[23] Figure 5 depicts the total wave power (I) as a function of ω. It is clear that the transversal wave is significantly more intense than the compressive wave. The transversal wave power peaks at $\omega \simeq 0.5$, while the compressive wave power peaks at $\omega \simeq 0.25$, 0.5, and 0.75. Note that the first peak of the compressive wave, at frequency $\omega \simeq 0.25$, coincides with the first minimum of the

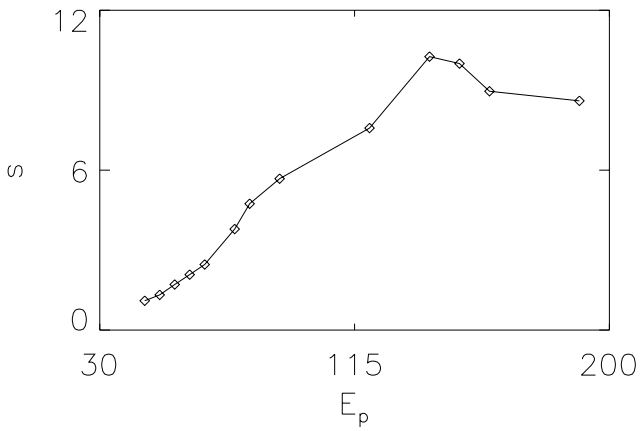

Figure 3. The *e*-folding distances obtained from the simulation for bow shock diffuse ions.

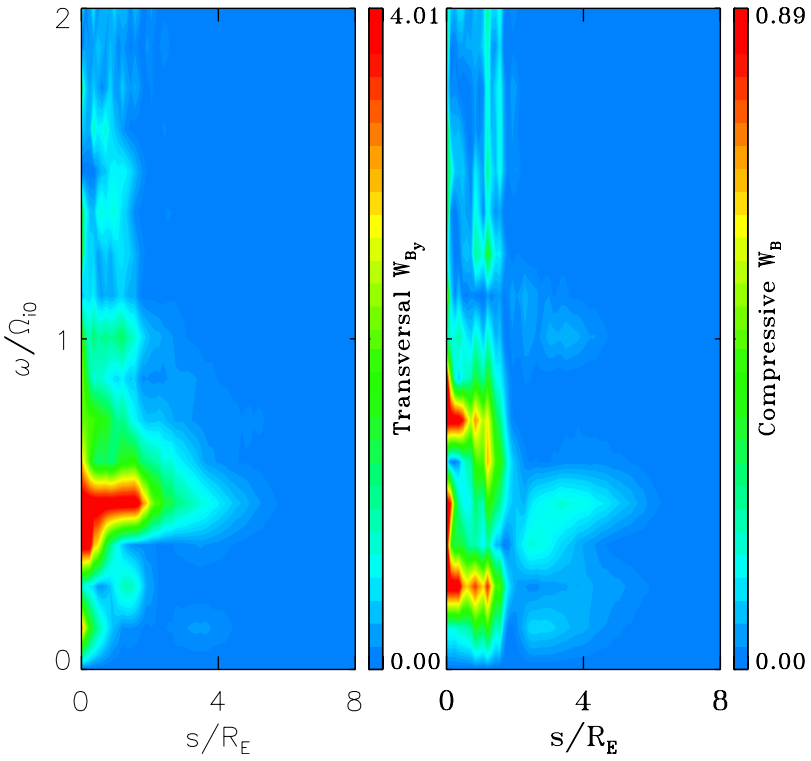

Figure 4. Wave energy as a function of the distance s to the foreshock and wave frequency ω for (left) transversal and (right) compressive waves.

transversal component. Both wave power intensities can be fitted into a power law ($\sim\omega^{-\gamma}$), with index $\gamma \simeq 2$.

3.3. Ion Signatures in the Magnetosheath and Cusp

[24] Figure 6 shows ion distribution and energy spectra at $t = 100$ at two locations, one in the magnetosheath and the other in the low-altitude cusp as marked by C and D in Figure 1, respectively. The ion distribution in the magnetosheath (point C) is nearly isotropic. The magnetosheath ions contain a Maxwellian core distribution with temperature $T_i \simeq 5$ and a nonthermal "tail" with energies $E_p \simeq 100-600$. This energetic spectrum can be described by an exponential form with the e-folding energy at $\sim$76, as shown in red in Figure 6a. A similar ion spectrum also appears at the low-altitude cusp (point D). In this case, the e-folding energy is slightly higher at 89. At a higher altitude at $r = 8$ in the cusp (not shown), the core distribution is composed of two counterstreaming components, one with a positive parallel bulk velocity representing the precipitating magnetosheath particles and the other with a negative parallel bulk velocity corresponding to the ions mirrored at lower altitudes.

3.4. Cusp Waves

[25] In the simulation with IMF $B_y = 0$, the simulated cusp is nearly symmetric about the noon-meridian plane. Figure 7 shows plasma and magnetic field profile in the vicinity of the cusp in the noon-meridian plane at $t = 100$. The black lines in Figure 7 represent magnetic field line projection onto this plane. The region with enhanced $T_{\|}$ is highly correlated with the location of the cusp. The spatial distribution of the parallel ion temperature ($T_{\|}$) is highly correlated with the shape of the cusp. The particle density changes sharply across the boundary between the cusp and the magnetosphere, while V_x drops to $\sim$0 from the magnetosheath to the cusp. The total plasma pressure is

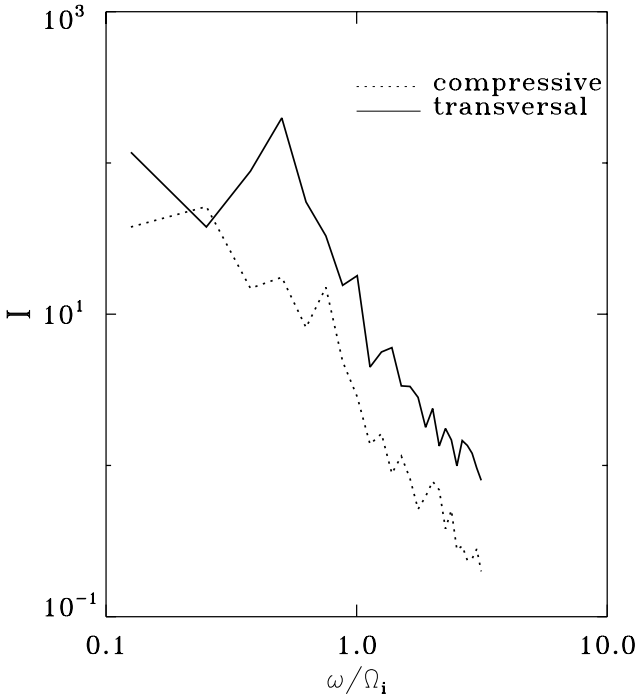

Figure 5. Wave power intensity versus frequency for transversal and compressive waves.

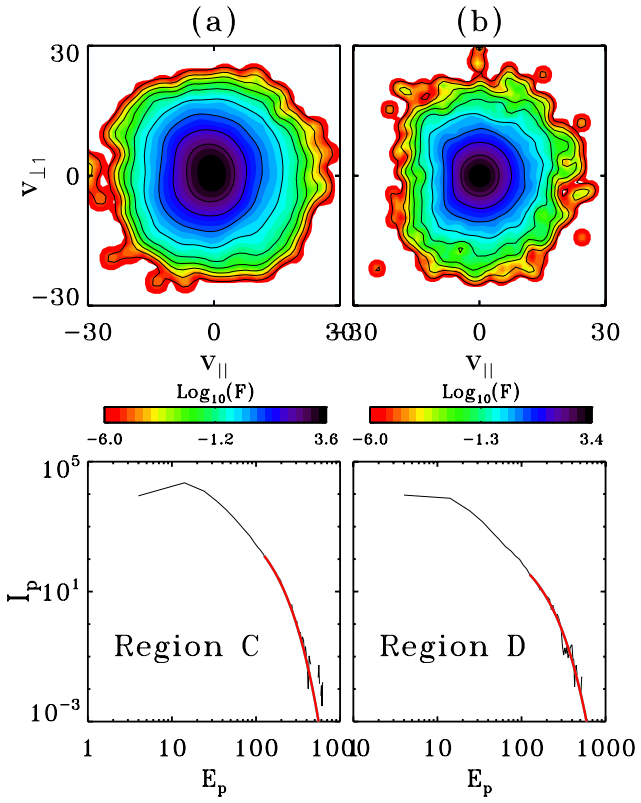

Figure 6. (top) Ion distributions in the $v_{||} - v_{\perp 1}$ plane and (bottom) ion energy spectra for ions in (a) region C in the magnetosheath and (b) region D in the cusp, indicated in Figure 1. Red curves indicate exponential fits for the energetic ion spectra.

anticorrelated with the magnetic field energy density (not shown). A similar correlation has also been reported by satellite observations [*Niehof et al.*, 2008].

[26] The latitudinal position of the cusp appears to oscillate with time. Figures 8a and 8b show the stack plots in time of ion density as a function of colatitude along r = 6.75 and r = 8.75, respectively, while Figure 8c shows the corresponding stack plot of density profiles as a function of r along $\theta = 105°$ in the vicinity of the foreshock. Latitudinal oscillation of the cusp can be clearly identified from locations of the density peak in the low-altitude cusp, as traced by the dashed line in Figure 8a. The oscillation period is roughly 20. This period is nearly the same as that of quasi-parallel shock reformation, as seen from the positions of the density enhancement around $r \simeq 12$ in Figure 8c. The position of the magnetopause, where the density drops around $r \simeq 10$, also oscillates correspondingly. A similar oscillation period is found in the high-altitude cusp shown in Figure 8b, but the oscillation of the outer cusp is related not only to the Q-|| shock, which generates pressure pulses, but also to the magnetic reconnection occurring at the high-latitude magnetopause.

[27] Like the upstream region, turbulence and waves exist in the cusp. Cusp waves consist of two components, the transversal and compressive waves. In the noon-meridian plane, the former is represented by the variations in B_y, and the latter by B. Figure 9 (left and middle) shows the wave density, derived from the magnetic field data within r = 6–15, $\theta = 30°$ in the noon-meridian plane for a period t = 50–100. The two vertical lines in these plots mark the positions of magnetopause and bow shock. Few waves appear upstream and immediate downstream from the near perpendicular shock. The wave power at the very low frequency in the cusp is more intense than that in the magnetosheath. The

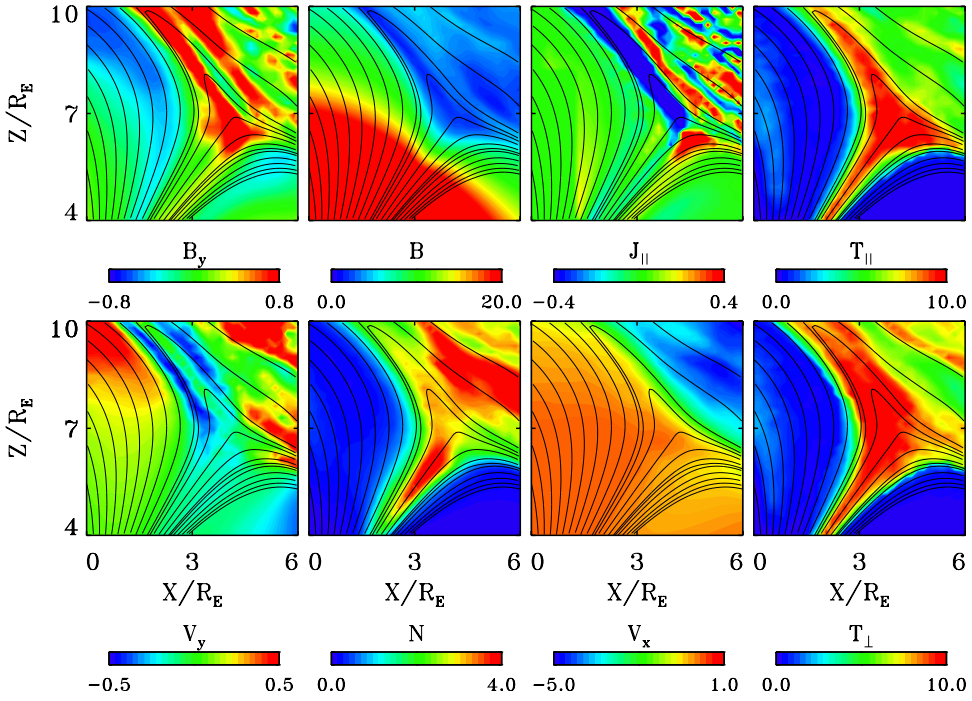

Figure 7. Contours of B_y, V_y, B, N, $J_{||}$, V_x, $T_{||}$, and $T_\perp$ in the noon-meridian plane around the cusp vicinity at t = 100.

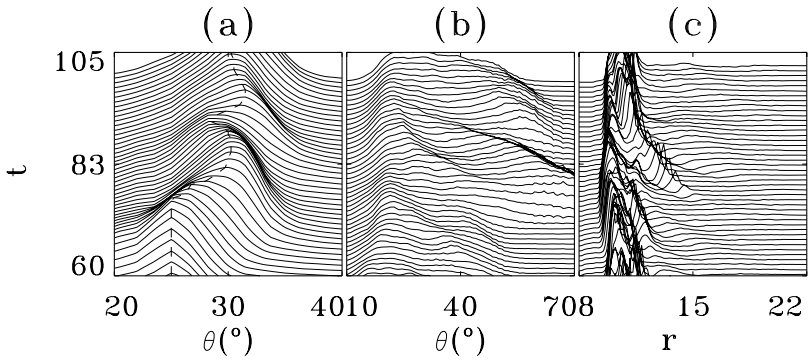

Figure 8. Stack plots in time of ion density as a function of θ in (a) low-altitude cusp at fixed $r = 6.75$ and (b) high-altitude cusp at $r = 8.75$ and as a function of r in (c) foreshock region at fixed $\theta = 105°$. Dashed line in Figure 8a represents the locations of density peak in the low-altitude cusp.

wave frequency in the cusp is below 0.4, while it is higher around 1.2 in the magnetosheath.

[28] The radial components of wave vectors, $\mathbf{k}_r$, in the cusp are roughly earthward for both transversal and compressive waves, indicative of upstream source. The value of k_r increases with altitude, e. g., $k_r \rightarrow 0$ at $r = 7 \pm 1.5$ to 3 at $r = 8.0 \pm 1.5$. The transversal wave in the cusp has a right-hand polarization.

[29] The two plots in Figure 9 (right) present the total wave power I in the cusp and magnetosheath, integrated over the corresponding ranges of r along $\theta = 30°$. In the cusp region within $r = 6$–9.5, the wave powers for the transversal and compressive waves are on the same order of magnitude. Both wave spectra can be well fitted with a power law $\sim\omega^{-\gamma}$, with the spectral index $\gamma = 3.5$. However, in the magnetosheath, within $r = 9.5$–13.2, the wave spectra are broken into two pieces at $\omega \simeq 1$, which is about one third of the local ion gyrofrequency. Only the spectra with $\omega > 1$ are power law ($\gamma \simeq 3.5$). For $\omega < 1$, the compressive wave is more intense than that of the transversal wave.

3.5. Cusp Energetic Ions

[30] As described in section 3.3, the energetic ion spectrum in the cusp is similar to those at the bow shock, foreshock, and magnetosheath. By tracing trajectories of the cusp energetic ions, it can shed some light on the origin of CEPs [*Lin et al.*, 2007]. Figure 10 shows a typical example of cusp energetic ions in the simulation from $t = 0$–100. Ion energy is indicated by the color of the 3-D trajectory according to the color scale. The locations of the bow shock

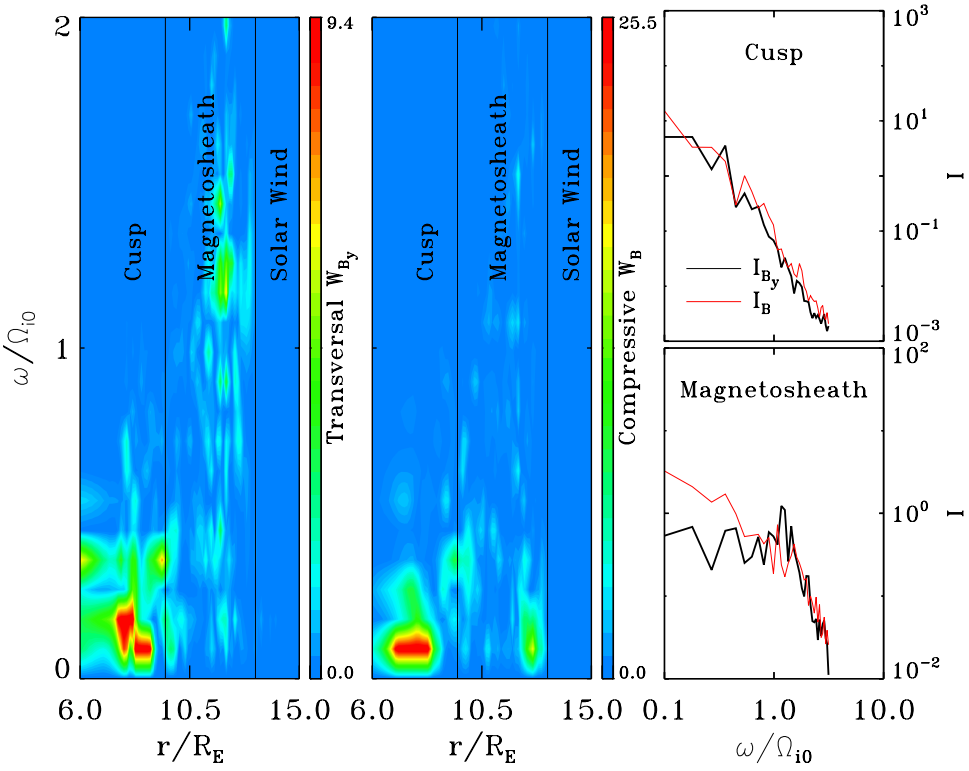

Figure 9. Wave energy spectrogram for (left) transversal and (middle) compressive waves and (right) wave spectra in the cusp and magnetosheath.

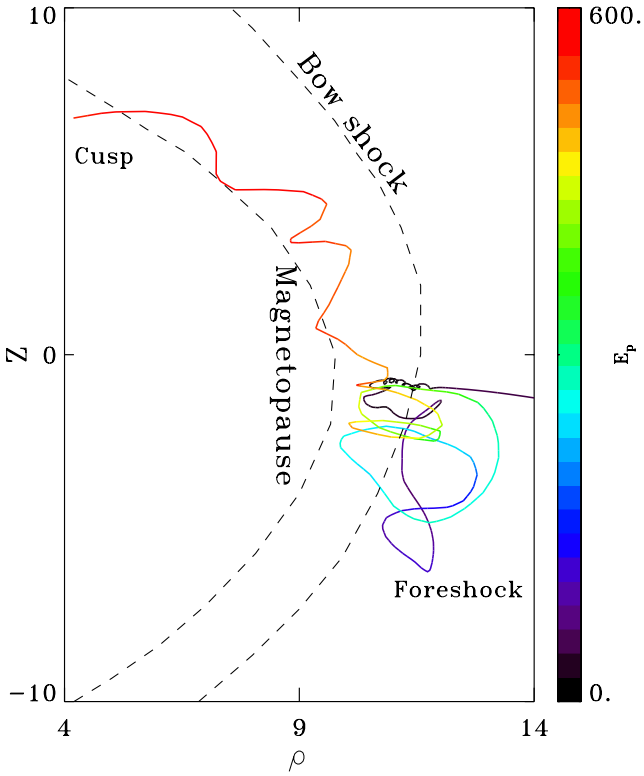

Figure 10. A typical trajectory of energetic ions in the ρ-z plane from $t = 0-100$ for ion transmitted into the cusp at $t = 100$, where $\rho = \sqrt{(x^2 + y^2)}$. Colors on the trajectory indicate the ion energy.

and magnetopause at $t = 100$ are marked by the dashed lines for reference. In this example the ion gains most of its energy nonadiabatically at the Q-|| shock and its vicinity. Ion energy remains nearly the same in the magnetosheath and cusp. Of all the cusp energetic ions, 90% particles are accelerated predominantly in the Q-|| shock region in this fashion.

[31] In addition to being bounced and accelerated in the shock, some of cusp energetic ions may also be deflected by the high-latitude reconnection and/or mirrored back from a lower altitude after precipitating into the inner cusp, as shown by *Lin et al.* [2007]. Although compressive and transversal waves are also found in the cusp, magnetosheath, and magnetic reconnection at the magnetopause, their contribution to the acceleration of individual energetic ions appears to be insignificant. Some solar wind ions are reflected by the quasi-perpendicular shock and later find their way to the subsolar bow shock region where the shock is quasi-parallel. They then get accelerated by the similar Fermi process shown in Figure 10, while the quasi-perpendicular shock appears not to be a sufficient source for the cusp energetic ions [*Lin et al.*, 2007].

4. Discussion

[32] In section 3, we have shown that the energetic ion spectra in the foreshock and cusp are well fitted in exponential form. The foreshock ion flux decreases with distance to the shock, with an energy-dependent e-folding distance. Two types of electromagnetic waves, (transversal and compressive) coexist with energetic ions in the foreshock and cusp regions.

[33] For typical solar wind parameters, solar wind energy $E_{sw} = 32$ used in the simulation is equivalent to about several keV. For example, E_{sw} is ~7.5 keV for solar wind density of 5 cm^{-3}, $M_A = 8$ and IMF $\simeq$ 15 nT. The maximum energy of CEPs ($E_{tail} \sim 20E_{sw}$) in the simulation, is thus estimated to be ~150 keV. As mentioned above, energetic ions exist at the foreshock, Q-|| shock, magnetosheath, and cusp and their energy spectra can be described by an exponential function with a single e-folding energy (~$3E_{sw}$ or 20 keV), indicative of a strong similarity of energetic ion spectra between foreshock and cusp.

[34] As expected in the bow shock acceleration, our simulation shows that diffuse ion flux decreases exponentially away from the shock. The patten of the relationship between the e-folding distance s_0 and particle energy E_p, as illustrated in Figure 3, is consistent with satellite observations [cf. *Trattner et al.*, 1994, Figure 7]. In both the observation and simulation, the e-folding distance roughly increases with the proton energy below 30 keV linearly and saturates at ~10 R_e above 30 keV.

[35] In addition, foreshock wave spectra from the simulation as shown, for example, in Figure 5 are also consistent with observations [cf. *Trattner et al.*, 1994, Figure 3]. In both the simulation and observations, the wave power of the transversal component substantially exceeds that of the compressive component. The power spectrum peaks at around $0.5\Omega_i$ in the simulation, while it peaks at 0.03 Hz in the observation.

[36] Theoretically, the coupling between the hydromagnetic waves and diffuse ions has been investigated using a self-consistent quasi-linear model [*Lee*, 1982]. The relationship between wave energy density w_B and diffuse ion energy density w_p is the following [*Möbius et al.*, 1987]:

$$w_B = 6.57[(1/3)(1 - N_u/N_d)]^2 V_{A0}/V_{sw} w_P, \qquad (1)$$

where N_u/N_d is the ratio of upstream to downstream plasma densities, and V_{sw} is the solar wind velocity. Such a result is derived from a model of describing interaction between energetic ions and waves. This relationship has been confirmed by observations from AMPTE/IRM [*Trattner et al.*, 1994]. To further evaluate bow shock acceleration in the simulation, equation (1) is examined using simulation outputs to calculate the wave energy density $w_B(sim)$ to be compared with the predicted value $w_B(pre)$. The results in the above typical simulation case are shown in Figure 11. In general, there is a good correlation between the two quantities, with the Pearson correlation coefficient 0.78, indicative of bow shock diffuse ions are accelerated by waves via the Fermi mechanism in the simulation.

[37] In the simulation, both the transversal and the compressive wave spectra in the cusp can be described by a power law, with the spectrum index $\gamma \simeq 3.5$. Similar spectra in the range of 0.01–1 Hz have been represented in the vicinity of cusp [*Chen and Fritz*, 1998; *Le et al.*, 2001]. The observed compressive wave power is on the same order of the transversal wave power. However, the spectral index in the observed spectra is about 2.5, smaller than that in our simulation. This difference may be due to that energetic magnetospheric ions

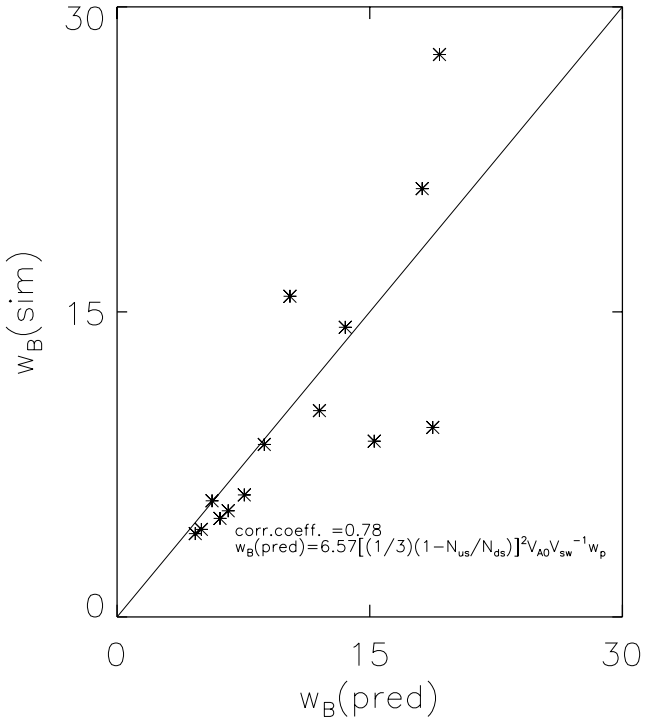

Figure 11. The wave energy density $w_B(sim)$ obtained in the simulation versus the predicted value from theory $w_B(pred)$.

and their effect on cusp waves are not included in the model. Although temperature anisotropy exists at the tailward boundary of the cusp, there appears no additional waves generated by the ion temperature anisotropy in the simulation. By comparing magnetic field profile at each simulation time (not shown), the source of cusp waves is revealed. They are generated upstream from the shock, propagating through the shock and magnetosheath and then into the cusp.

[38] All the spectral characteristics of bow shock diffuse ions and waves, and cusp energetic ions and waves discussed above, seem to suggest that the Q-∥ shock is a main source region of CEPs. More evidence from the simulation supports this notion as described below. The fact that less than 10% of energetic ions are trapped in the cusp for a time longer than one bounce period in this simulation indicates an insufficient time to accelerate the CEPs locally in the cusp. The most definitive evidence for the bow shock source is that the CEPs gain nearly all of their energy at the shock in the simulation as shown, for example, in Figure 10. Note that magnetosphere energetic ions are not included in this simulation and they may account for more energetic ion flux in the observations.

[39] While the simulation results are scaled by the actual physical quantities, the solar wind ion inertial length and Alfvén speed used in the simulation are larger than the real values. Further studies are required to determine the effect of spatial scaling on the bow shock acceleration and CEPs on a global scale.

5. Summary

[40] A 3-D global hybrid simulation is carried out to investigate energetic ions and electromagnetic waves at the Q-∥ bow shock and cusp for a typical IMF configuration during the CEP events. The following results are obtained from the simulation.

[41] 1. Transversal and compressive electromagnetic waves are generated at the Q-∥ shock and foreshock, where the reflected ion beams interact with the incoming solar wind. The transversal wave is the dominant component. Its power intensity is well described by a power law. These characteristics are consistent with satellite observations.

[42] 2. Ions are accelerated and heated by the Q-∥ shock. The bow shock ions possess a diffuse ion distribution with an exponential energy spectrum. Foreshock ion flux is also scaled exponentially by the field-aligned distance to the shock with an *e*-folding distance of 3–9 for various ion energies. Foreshock wave power and diffuse ion flux are well correlated as expected in shock acceleration. These simulation results agree well with bow shock observation.

[43] 3. Energetic ions also exist downstream from the Q-∥ shock in the magnetosheath and cusp. These ions exhibit an exponential spectrum similar to the bow shock diffuse ions, although ion distributions appear different in these regions. The "core" ion distribution in the outer cusp is composed of two counterstreaming components.

[44] 4. The funnel-shaped cusp can be clearly identified by the plasma temperature parallel to the magnetic field. The latitudinal position of the cusp oscillates. This oscillation, as well as the cusp and magnetosheath waves, are related to the pressure pulses at Q-∥ shock and the high-latitude magnetic reconnection. The power intensity of the transversal cusp wave is on the same order of magnitude as the compressive wave. Both wave spectra can be well fitted by a power law.

[45] 5. All the CEPs with energy ~20 E_{sw} gain their energy predominantly in the vicinity of Q-∥ shock. The ions are accelerated nonadiabatically by a Fermi-type mechanism when they bounce between the upstream and downstream waves. Waves in the magnetosheath and cusp as well as magnetic reconnection appear insignificant in accelerating these particles.

[46] **Acknowledgments.** This work was supported by NSF grant ATM-0213931 to Auburn University and in part by NSF grant ATM-0242427 and NASA grant NNX07AG09G to UAH. Computer resources were provided by the Arctic Region Supercomputer Center.

[47] Amitava Bhattacharjee thanks Dan Winske and Nick Omidi for their assistance in evaluating this paper.

References

Blake, J. B. (1999), Comment on "Cusp: A new acceleration region of the magnetosphere" by J. Chen et al., *Czech. J. Phys.*, *49*, 675.

Blanco-Cano, X., N. Omidi, and C. T. Russell (2006), Macrostructure of collisionless bow shocks: 2. ULF waves in the foreshock and magnetosheath, *J. Geophys. Res.*, *111*, A10205, doi:10.1029/2005JA011421.

Cargill, P. J., et al. (2005), Cluster at the magnetospheric cusps, *Spac. Sci. Rev.*, *118*, 321.

Cao, J. B., H. S. Fu, T. L. Zhang, H. Reme, I. Dandouras, and E. Lucek (2009), Direct evidence of solar wind deceleration in the foreshock of the Earth, *J. Geophys. Res.*, *114*, A02207, doi:10.1029/2008JA013524.

Chang, S.-W., et al. (1998), Cusp energetic ions: A bow shock source, *Geophys. Res. Lett.*, *25*, 3729.

Chang, S.-W., J. D. Scudder, J. F. Fennell, R. Friedel, R. P. Lepping, C. T. Russell, K. J. Trattner, S. A. Fuselier, W. K. Peterson, and H. E. Spence (2000), Energetic magnetosheath ions connected to the Earth's bow shock: Possible source of cusp energetic ions, *J. Geophys. Res.*, *105*, 5471.

Chang, S.-W., J. D. Scudder, K. Kudela, H. E. Spence, J. F. Fennell, R. P. Lepping, R. P. Lin, and C. T. Russell (2003), Reply to comment by

J. Chen et al. on "MeV magnetosheath ions energized at the bow shock", *J. Geophys. Res.*, *108*(A8), 1312, doi:10.1029/2002JA009724.
Chen, J., and T. A. Fritz (1998), Correlation of cusp MeV helium with turbulent ULF power spectra and its implications, *Geophys. Res. Lett.*, *25*, 4113.
Chen, J., T. A. Fritz, R. B. Sheldon, H. E. Spence, W. N. Spjeldvik, J. F. Fennell, and S. Livi (1997), A new, temporarily confined population in the polar cap during the August 27, 1996 geomagnetic field distortion period, *Geophys. Res. Lett.*, *24*, 1447.
Chen, J., T. A. Fritz, R. B. Sheldon, H. E. Spence, W. N. Spjeldvik, J. F. Fennell, S. Livi, C. T. Russell, J. S. Pickett, and D. A. Gurnett (1998), Cusp energetic particle events: Implications for a major acceleration region of the magnetosphere, *J. Geophys. Res.*, *103*, 69.
Chen, J., T. A. Fritz, and R. B. Sheldon (2003), Comment on "MeV magnetosheath ions energized at the bow shock" by S.-W. Chang et al., *J. Geophys. Res.*, *108*(A8), 1311, doi:10.1029/2002JA009634.
Ellison, D. C., et al. (1990), Particle injection and acceleration at Earth's bow shock: Comparison of upstream and downstream events, *Astrophys. J.*, *352*, 376.
Fenrich, F. R., J. G. Luhmann, J. A. Fedder, S. P. Slinker, and C. T. Russell (2001), A global MHD and empirical magnetic field model investigation of the magnetospheric cusp, *J. Geophys. Res.*, *106*, 18,789.
Fritz, T. A., and J. Chen (1999), Reply, *Geophys. Res. Lett.*, *26*, 1363.
Fuselier, S. A., M. F. Thomsen, F. M. Ipavich, and W. K. H. Schmidt (1995), Suprathermal He^{2+} in the Earth's foreshock region, *J. Geophys. Res.*, *100*, 17,107.
Giacalone, J., D. Burgess, S. J. Schwartz, and D. C. Ellison (1992), Hybrid simulations of protons strongly accelerated by a parallel collisionless shock, *Geophys. Res. Lett.*, *19*, 433.
Gosling, J. T., M. F. Thomsen, S. J. Bame, and C. T. Russell (1989), On the source of diffuse, suprathermal ions observed in the vicinity of the Earth's bow shock, *J. Geophys. Res.*, *94*, 3555.
Heikkila, W. J., and J. D. Winningham (1971), Penetration of magnetosheath plasma to low altitudes through the dayside magnetospheric cusps, *J. Geophys. Res.*, *76*, 883.
Ipavich, F. M., M. Scholer, and G. Gloeckler (1981), Temporal development of composition, spectra, and anisotropies during upstream particle events, *J. Geophys. Res.*, *86*, 11,153.
Lavraud, B., et al. (2005), Cluster observes the high-latitude cusp region, *Surv. Geophys.*, *26*, 135.
Le, G., X. Blanco-Cano, C. T. Russell, X.-W. Zhou, F. Mozer, K. J. Trattner, S. A. Fuselier, and B. J. Anderson (2001), Electromagnetic ion cyclotron waves in the high-altitude cusp: Polar observations, *J. Geophys. Res.*, *106*, 19,067.
Lee, M. A. (1982), Coupled hydromagnetic wave excitation and ion acceleration upstream of the Earth's bow shock, *J. Geophys. Res.*, *87*, 5063.
Lin, Y., and X. Y. Wang (2005), Three-dimensional global hybrid simulation of dayside dynamics associated with the quasi-parallel bow shock, *J. Geophys. Res.*, *110*, A12216, doi:10.1029/2005JA011243.
Lin, Y., and X. Y. Wang (2006), Formation of dayside low-latitude boundary layer under northward interplanetary magnetic field, *Geophys. Res. Lett.*, *33*, L21104, doi:10.1029/2006GL027736.
Lin, Y., X. Y. Wang, and S.-W. Chang (2007), Connection between bow shock and cusp energetic ions, *Geophys. Res. Lett.*, *34*, L11107, doi:10.1029/2007GL030038.
Möbius, E., M. Scholer, N. Sckopke, H. Lühr, G. Paschmann, and D. Hovestadt (1987), The distribution function of diffuse ions and the magnetic field power spectrum upstream of Earth's bow shock, *Geophys. Res. Lett.*, *14*, 681.
Niehof, J. T., T. A. Fritz, R. H. W. Friedel, and J. Chen (2008), Interdependence of magnetic field and plasma pressures in cusp diamagnetic cavities, *Geophys. Res. Lett.*, *35*, L11101, doi:10.1029/2008GL033589.
Scholer, M., and T. Terasawa (1990), Ion reflection and dissipation at quasi-parallel collisionless shocks, *Geophys. Res. Lett.*, *17*, 119.
Sheldon, R., J. Chen, and T. A. Fritz (2003), Comment on "Origins of energetic ions in the cusp" by K. J. Trattner et al., *J. Geophys. Res.*, *108*(A7), 1302, doi:10.1029/2002JA009575.
Siscoe, G., N. Crooker, K. Siebert, N. Maynard, D. Weimer, and W. White (2005), Cusp geometry in MHD simulations, *Surv. Geophys.*, *26*, 387.
Siscoe, G., Z. Kaymaz, and Y. V. Bogdanova (2007), Magnetospheric cusps under extreme conditions: Cluster observations and MHD simulations compared, *Sol. Phys.*, *244*, 189.
Smith, M. F., and M. Lockwood (1996), Earth's magnetospheric cusps, *Rev. Geophys.*, *34*, 233.
Swift, D. W. (1996), Use of a hybrid code for a global-scale plasma simulation, *J. Comput. Phys.*, *126*, 109.
Trattner, K. J., and M. Scholer (1994), Diffuse minor ions upstream of simulated quasi-parallel shocks, *J. Geophys. Res.*, *99*, 6637.
Trattner, K. J., E. Möbius, M. Scholer, B. Klecker, M. Hilchenbach, and H. Lühr (1994), Statistical analysis of diffuse ion events upstream of the Earth's bow shock, *J. Geophys. Res.*, *99*, 13,389.
Trattner, K. J., S. A. Fuselier, W. K. Peterson, and S.-W. Chang (1999), Comment on "Correlation of cusp MeV helium with turbulent ULF power spectra and its implications" by J. Chen and T. A. Fritz, *Geophys. Res. Lett.*, *26*, 1361.
Trattner, K. J., S. A. Fuselier, W. K. Peterson, S.-W. Chang, R. Friedel, and M. R. Aellig (2001), Origins of energetic ions in the cusp, *J. Geophys. Res.*, *106*, 5967.
Trattner, K. J., S. A. Fuselier, W. K. Peterson, S.-W. Chang, R. Friedel, and M. R. Aellig (2003), Reply to comment by R. Sheldon, J. Chen, and T. A. Fritz on "Origins of energetic ions in the cusp", *J. Geophys. Res.*, *108*(A7), 1303, doi:10.1029/2002JA009781.
Tsyganenko, N. A., and C. T. Russell (1999), Magnetic signatures of the distant polar cusps: Observations by polar and quantitative modeling, *J. Geophys. Res.*, *104*, 24,939.
Vogiatzis, I. I., T. E. Sarris, E. T. Sarris, O. Santolík, I. Dandouras, P. Robert, T. A. Fritz, Q.-C. Zong, and H. Zhang (2008), Cluster observations of particle acceleration up to supra-thermal energies in the cusp region related to low-frequency wave activity—Possible implications for the substorm initiation process, *Ann. Geophys.*, *26*, 653.
Wang, X. Y., and Y. Lin (2003), Generation of nonlinear Alfvén and magnetosonic waves by beam-plasma interaction, *Phys. Plasmas*, *10*, 3528.
Zong, Q.-G., T. A. Fritz, H. Spence, H. U. Frey, S. B. Mende, A. Korth, and P. W. Daly (2005), Reverse convection and cusp proton aurora: Cluster, polar and image observation, *Adv. Space Res.*, *36*, 1779.

S.-W. Chang, National Space Science and Technology Center, VP62, 320 Sparkman Drive, Huntsville, AL 35805, USA. (shen.chang@nasa.gov)
Y. Lin and X. Y. Wang, Physics Department, Auburn University, 206 Allison Laboratory, Auburn, AL 36849-5311, USA. (ylin@physics.auburn.edu; xywang@physics.auburn.edu)